Chinese Chemical Letters 36 (2025) 110349

Contents lists available at ScienceDirect

Chinese Chemical Letters

journal homepage: www.elsevier.com/locate/cclet

Highly-stable cesium lead halide perovskite $CsPbBr_3/CsPb_2Br_5$ heteronanocrystals in zeolitic imidazolate framework-8 for antibiotic photodegradation

Le Han[a], Zhou Yuan[a], Bohan Li[a], Yuchi Zhang[a], Lin Yang[a], Yan Xu[a,b,*]

[a] Department of Chemistry, College of Sciences, Northeastern University, Shenyang 110819, China
[b] Foshan Graduate School of Innovation, Northeastern University, Foshan 528311, China

ARTICLE INFO

Article history:
Received 8 May 2024
Revised 18 July 2024
Accepted 17 August 2024
Available online 17 August 2024

Keywords:
Perovskite
Heterojunction
High stability
Tetracycline
Aqueous photocatalysis

ABSTRACT

Metal halide perovskite nanocrystals (MHP NCs) are of great candidates in photocatalytic applications due to their extreme light utilization efficiency. However, the instability towards humid environment severely restrict their practical application. Herein, the $CsPbBr_3/CsPb_2Br_5$ heteronanocrystals (HNCs) were successfully encapsulated into ZIF-8 through a thermal injection method *via* controlling the molar ratio of Cs^+/Pb^{2+}. The surface of ZIF-8 was then modified with hydrophobic copolymer of poly(methyl methacrylate) (PMMA) to improve the water stability. Benefiting from the intimate interfacial interaction and staggered energy band structure, the type-II heterojunction of $CsPbBr_3/CsPb_2Br_5$ guarantees efficient separation and migration of photogenerated electron/hole pairs. Meanwhile, the formation of Z-scheme heterojunction between ZIF-8 and $CsPbBr_3/CsPb_2Br_5$ HNCs contributes to the adsorption and enrichment of pollutants, further accelerates the photocatalytic antibiotic degradation efficiency towards tetracycline hydrochloride (TCH) in aqueous solution. Nearly 87% of TCH (40 mg/L, 50 mL) was degraded by 40 mg catalyst within 100 min. This work offers a feasible approach in assembling high-performance MHP NCs-based efficient photocatalyst with expanding application in aqueous solution.

Metal halide perovskite nanocrystals (MHP NCs) have garnered great attention in photocatalysis due to their unique electronic energy band structure of appropriate redox potential and outstanding light absorption and charge transfer efficiency [1–4]. Recently, great catalytic performances of MHP NCs photocatalysts on water splitting, CO_2 reduction, dye and antibiotic degradation have been extensively investigated [5–8]. However, MHP NCs are sensitive to polar solvent and hyperthermia on accounts of the high delocalization activity and low lattice formation energy of surface ions, which severely hinder the photocatalytic applications [9,10]. Additionally, environmental pollution caused by antibiotic contamination is a growing problem. The chemical stability and inherent resistance of tetracycline hydrochloride (TCH) molecules have led to their widespread accumulation in aquatic environments, causing serious impacts on ecosystems and human health [11]. Therefore, it is significant to explore novel MHP NCs-based photocatalysts exhibiting high performance for TCH degradation in aqueous solution.

Several attempts have been implemented to overcome the drawbacks of MHP NCs, involving surface modification, element doping, and heterostructure construction [12]. Among them, the synergistic effect in heterostructure holds advantages in accelerating the separation and transfer of charge carriers, and thus enables the collaboration of each component to promote light adsorption and improve degradation efficiency [13]. On this respect, MHP NCs have been widely integrated with diverse components such as Cs_4PbBr_6, $CsPb_2Br_5$, and Rb_4PbBr_6 at the nanoscale to create new heteronanocrystals (HNCs) with well-defined interfaces and superior properties [14–22]. Two dimensional layered $CsPb_2Br_5$ perovskite was considered to be a good candidate for construction of heterojunction with $CsPbBr_3$ NCs due to its minimal lattice mismatch [23]. Several strategies on assembly of $CsPbBr_3/CsPb_2Br_5$ heterostructures have been developed, in which the close contact interface in $CsPbBr_3/CsPb_2Br_5$ is conducive for the photocatalytic reaction on accounts of unique internal charge transfer mechanism [23–25]. However, lack of molecular enrichment of pollutants remarkably restrict the photocatalytic properties of $CsPbBr_3/CsPb_2Br_5$ HNCs in aqueous solution [26]. Encapsulation of $CsPbBr_3/CsPb_2Br_5$ HNCs in porous materials is a promising way to overcome this restriction [27,28].

* Corresponding author.
E-mail address: xuyan@mail.neu.edu.cn (Y. Xu).

https://doi.org/10.1016/j.cclet.2024.110349
1001-8417/

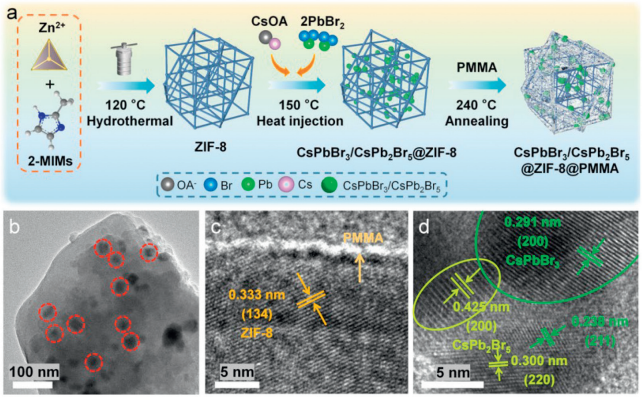

Fig. 1. (a) Schematic diagram for preparation of $CsPbBr_3/CsPb_2Br_5$@ZIF-8@PMMA. (b) TEM and (c, d) HRTEM of $CsPbBr_3/CsPb_2Br_5$@ZIF-8@PMMA composite.

Metal-organic frameworks (MOFs) are significant crystalline materials constructed from metal ions/metal clusters with organic linkers through coordination bonding effect [29]. Zeolitic imidazolate framework (ZIF-8) is a subtype of MOFs assembled from Zn^{2+} ions and 2-methylimidazole, exhibiting outstanding chemical stability [30]. Moreover, ZIF-8 has a positive valence band, showing opportunity to assemble a Z-scheme heterojunction with MHP NCs to achieve an efficient separation of photoexcited electrons and holes [31]. However, numerous amounts of water/oxygen molecules can come through the pore structure of ZIF-8 to decompose $CsPbBr_3$ NCs ascribing to its incompletely isolation from the surroundings [32,33]. Coating a hydrophobic polymer on the surface of MOF to construct double-protected shells over $CsPbBr_3$ NCs is a promising approach to elevate the stability [34].

In this work, the $CsPbBr_3/CsPb_2Br_5$ HNCs were successfully encapsulated into ZIF-8 by capitalizing on the spatial constraint effect of MOF and controlling the molar ratio of Cs^+/Pb^{2+} precursors under a thermal injection condition. Subsequently, the surface of $CsPbBr_3/CsPb_2Br_5$@ZIF-8 was modified with poly(methyl methacrylate) (PMMA) polymer to form $CsPbBr_3/CsPb_2Br_5$@ZIF-8@PMMA composite. The inner $CsPbBr_3/CsPb_2Br_5$ HNCs with excellent optoelectronic properties can facilitate the transfer of photogenerated electrons and holes, contributing to the high photocatalytic efficiency. The ZIF-8 shell can help to enrich TCH species around the catalyst, and the outmost modification of PMMA afford the composite hydrophobicity. As a result, the $CsPbBr_3/CsPb_2Br_5$@ZIF-8@PMMA composite exhibited excellent TCH degradation efficiency (~87%) in aqueous solution within 100 min under visible light irradiation. This work provides a simple and feasible approach on assembling water-stable MHP NCs photocatalysts for effective degradation of antibiotics in aqueous solution.

The preparation process of $CsPbBr_3/CsPb_2Br_5$@ZIF-8@PMMA composite is illustrated in Fig. 1a. The encapsulation of $CsPbBr_3/CsPb_2Br_5$ in ZIF-8 were prepared through an *in-situ* hot injection method. Subsequently, $CsPbBr_3/CsPb_2Br_5$@ZIF-8 and PMMA powder in a certain mass ratio were fully milled and then annealed under nitrogen atmosphere at 240 °C (higher than the melting point of PMMA) for 30 min to obtain the $CsPbBr_3/CsPb_2Br_5$@ZIF-8@PMMA composite. Transmission electron microscopy (TEM) and high-resolution transmission electron microscopy (HRTEM) were tested to characterize the internal structure of $CsPbBr_3/CsPb_2Br_5$@ZIF-8@PMMA. The TEM image in Fig. 1b shows the distribution of $CsPbBr_3/CsPb_2Br_5$ HNCs (red dotted circle) encapsulated in ZIF-8. From the HRTEM image shown in Fig. 1c, the ZIF-8 exhibited a clear lattice fringe with a 0.333 nm spacing corresponds to the (134) crystal plane, and the PMMA polymer layer was homogeneously coated on the surface of ZIF-8 [34]. In Fig. 1d, the lattice spacings of 0.291 and 0.238 nm for $CsPbBr_3$, and that of $CsPb_2Br_5$ (0.425, 0.300 nm) match well with the (200), (211) crystal planes of $CsPbBr_3$ and that of (200), (220) for $CsPb_2Br_5$, respectively. This further indicates the successful incorporation of $CsPbBr_3/CsPb_2Br_5$ HNCs into ZIF-8.

The morphologies of ZIF-8, $CsPbBr_3/CsPb_2Br_5$@ZIF-8 and $CsPbBr_3/CsPb_2Br_5$@ZIF-8@PMMA were characterized by scanning electron microscopy (SEM) and the results are shown in Figs. 2a–c. The ZIF-8 exhibits an interpenetrating twin morphology with a microparticle size of <2.0 μm (Fig. 2a). The morphology of ZIF-8 did not change after encapsulation of $CsPbBr_3/CsPb_2Br_5$ HNCs, demonstrating that the thermal injection process did not cause the ZIF-8 crystal structure to collapse (Fig. 2b). Then, the $CsPbBr_3/CsPb_2Br_5$@ZIF-8 was mixed with PMMA powder in nitrogen atmosphere and annealed for 30 min at 240 °C to obtain $CsPbBr_3/CsPb_2Br_5$@ZIF-8@PMMA composite. As shown in Fig. S1 (Supporting Information), the morphology of PMMA is spherical with the size of about 10 μm. After annealing treatment the spherical PMMA polymer melted and disappeared after it was uniformly coated over ZIF-8 (Fig. 2c). The corresponding schematic structure diagram of ZIF-8, $CsPbBr_3/CsPb_2Br_5$@ZIF-8 and $CsPbBr_3/CsPb_2Br_5$@ZIF-8@PMMA are displayed in Figs. 2a–c. X-ray diffraction (XRD) patterns of ZIF-8, $CsPbBr_3/CsPb_2Br_5$@ZIF-8 and $CsPbBr_3/CsPb_2Br_5$@ZIF-8@PMMA were recorded in Fig. 2d. The XRD peaks of ZIF-8 located at 2θ of 7.4°, 10.4°, 12.7°, 14.7°, 16.4°, 18.0° and 22.1° can be indexed into the (011), (002), (112), (022), (013), (222) and (114) crystal planes, respectively, confirming the phase purity [35]. The appearance of diffraction peaks of cubic $CsPbBr_3$ (JCPDS No. 54–0752) and tetragonal $CsPb_2Br_5$ (JCPDS No. 25–0211) in $CsPbBr_3/CsPb_2Br_5$@ZIF-8 composite proved the successful encapsulation of $CsPbBr_3/CsPb_2Br_5$ HNCs in ZIF-8. The XRD pattern of $CsPbBr_3/CsPb_2Br_5$@ZIF-8@PMMA was consistent with that of $CsPbBr_3/CsPb_2Br_5$@ZIF-8, demonstrating that the PMMA polymer coating has no effect on the structure stability and crystallinity. Elemental mapping images of $CsPbBr_3/CsPb_2Br_5$@ZIF-8@PMMA in the selected area were recorded (Figs. 2e–j), confirming the coexistence and uniform distribution of Cs, Pb, Br, Zn, N and O elements in the material.

Fourier transform infrared spectroscopy (FT-IR) spectra were recorded to further investigate the surface functional groups and ascertain whether PMMA was successfully coated on $CsPbBr_3/CsPb_2Br_5$@ZIF-8 composite. As shown in Fig. 3a, the peak located at 426 cm^{-1} corresponds to Zn-N stretching vibration, and the peaks located at 995, 1147, and 1423 cm^{-1} correspond to C–N stretching vibrations. The peak at 2930 cm^{-1} is the aliphatic C–H stretching vibration in 2-methylimidazole and the peak at 1584 cm^{-1} is related to that of C=N [36]. Additionally, the peaks at 2994 and 1737 cm^{-1} can be attributed to the stretching vibrations of the C–H bond and C=O bond in PMMA, respectively. The PMMA also exhibits additional vibration bands at 1447, 751, 1245 and 1143 cm^{-1} [37]. It was evident that the PMMA polymer was successfully grafted onto ZIF-8 to form $CsPbBr_3/CsPb_2Br_5$@ZIF-8@PMMA composite.

N_2 adsorption-desorption isotherms of ZIF-8, $CsPbBr_3/CsPb_2Br_5$@ZIF-8 and $CsPbBr_3/CsPb_2Br_5$@ZIF-8@PMMA composite were then measured (Fig. 3b) and the detailed data are collected in Table S1 (Supporting information). The $CsPbBr_3/CsPb_2Br_5$@ZIF-8 composite features a decreased BET surface area (82.514 m^2/g) and pore volume (0.053 cm^3/g) in comparison to that of ZIF-8 (436.315 m^2/g for BET and 0.233 cm^3/g for pore volume) due to the encapsulation of $CsPbBr_3/CsPb_2Br_5$ HNCs in ZIF-8. While the structural porosity is significantly promoted after PMMA network structure coating on $CsPbBr_3/CsPb_2Br_5$@ZIF-8, and the specific surface area and pore volume of $CsPbBr_3/CsPb_2Br_5$@ZIF-8@PMMA are 162.015 m^2/g and 0.097 cm^3/g, respectively. Furthermore, the pore size distribution

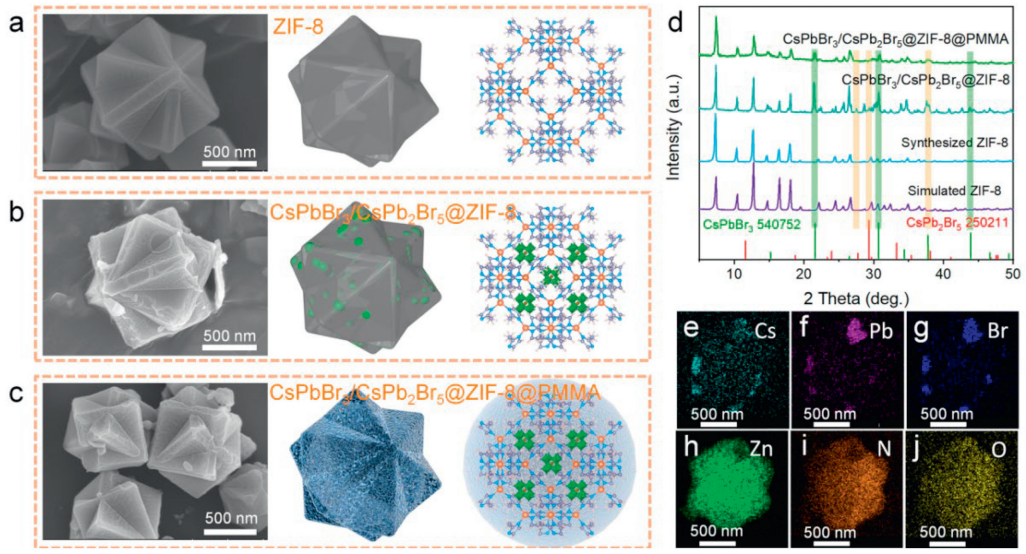

Fig. 2. SEM images, corresponding schematic diagram and structure diagram of (a) ZIF-8, (b) $CsPbBr_3/CsPb_2Br_5$@ZIF-8 and (c) $CsPbBr_3/CsPb_2Br_5$@ZIF-8@PMMA composite. (d) XRD patterns and energy dispersive spectrometry (EDS) mapping of (e) Cs, (f) Pb, (g) Br, (h) Zn, (i) N, and (j) O, respectively.

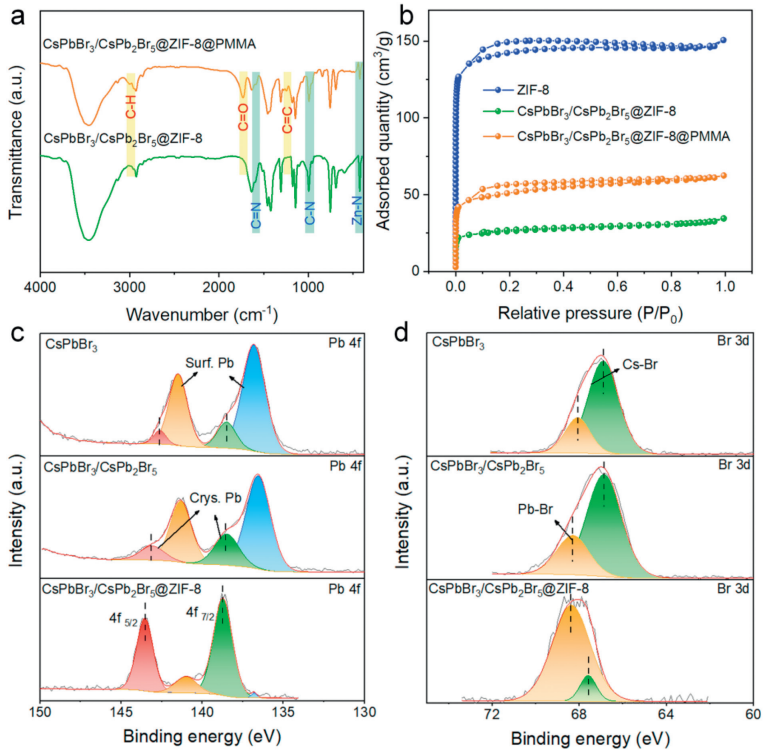

Fig. 3. (a) FT-IR spectra of $CsPbBr_3/CsPb_2Br_5$@ZIF-8 and $CsPbBr_3/CsPb_2Br_5$@ZIF-8@PMMA. (b) N_2 adsorption-desorption isotherms of ZIF-8, $CsPbBr_3/CsPb_2Br_5$@ZIF-8 and $CsPbBr_3/CsPb_2Br_5$@ZIF-8@PMMA. XPS of (c) Pb 4f and (d) Br 3d for $CsPbBr_3$, $CsPbBr_3/CsPb_2Br_5$ and $CsPbBr_3/CsPb_2Br_5$@ZIF-8 samples.

of ZIF-8, $CsPbBr_3/CsPb_2Br_5$@ZIF-8, and $CsPbBr_3/CsPb_2Br_5$@ZIF-8@PMMA composite are evaluated through density functional theory (DFT), and the comparisons of data are listed in Table S1. The pore size distribution of $CsPbBr_3/CsPb_2Br_5$@ZIF-8 is also reduced compared to ZIF-8, attributing to the insertion of $CsPbBr_3/CsPb_2Br_5$ HNCs.

X-ray photoelectron spectroscopy (XPS) was used to analyze the surface chemical states. As shown in Fig. S2 (Supporting information), for high-resolution XPS pattern of Cs 3d, no significant change was found in $CsPbBr_3$, $CsPbBr_3/CsPb_2Br_5$ and $CsPbBr_3/CsPb_2Br_5$@ZIF-8 samples, indicating the weak interactions between Cs^+ and $PbBr_6^{4-}$ octahedron [38]. The peak differential analysis of Pb 4f was shown in Fig. 3c. The peaks at 138.7 and 143.5 eV with high binding energies correspond to the crystal Pb^{2+} ions, while the two peaks at 136.6 and 141.4 eV with low binding energies correspond to the surface Pb^{2+} ions [39]. In the $CsPbBr_3/CsPb_2Br_5$ HNCs, the XPS signal of crystal Pb^{2+} ions is increased, and that of the surface Pb^{2+} ions is attenuated, demonstrating the assembly of Pb-Br octahedron. In other words, the surface Pb^{2+} ions indicated the existence of surface halide vacancies defects, while they were considerably diminished after the formation of $CsPbBr_3/CsPb_2Br_5$ HNCs. The Br 3d spec-

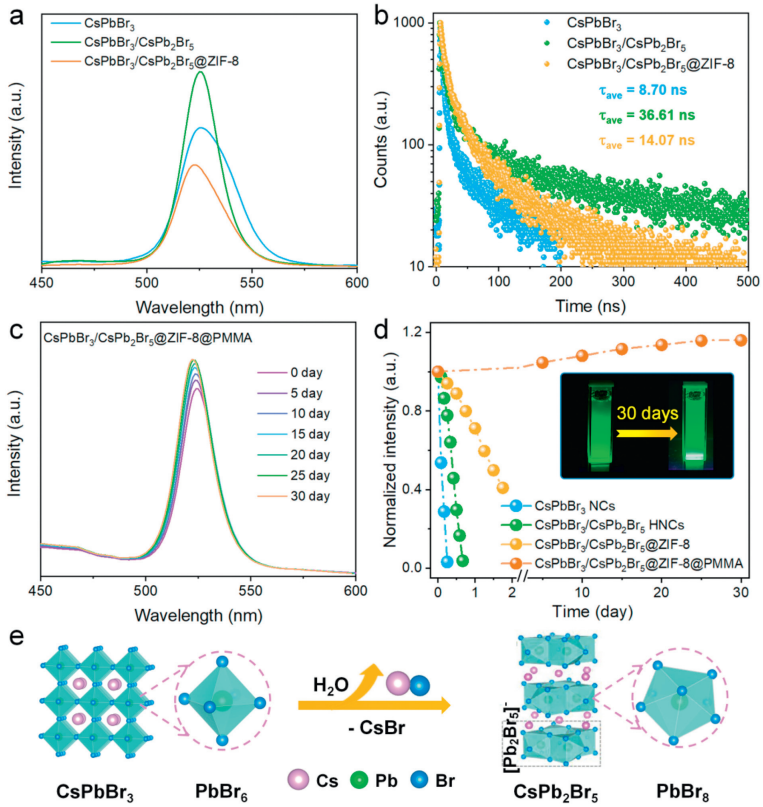

Fig. 4. (a) PL spectra (λ_{ex} = 365 nm), (b) PL decays lifetimes of $CsPbBr_3$@ZIF-8, $CsPbBr_3/CsPb_2Br_5$@ZIF-8 and $CsPbBr_3/CsPb_2Br_5$@ZIF-8@PMMA composite. (c) Water stability of $CsPbBr_3/CsPb_2Br_5$@ZIF-8@PMMA composite. (d) Comparison PL intensity stable of $CsPbBr_3$ NCs, $CsPbBr_3/CsPb_2Br_5$ HNCs, $CsPbBr_3/CsPb_2Br_5$@ZIF-8 and $CsPbBr_3/CsPb_2Br_5$@ZIF-8@PMMA samples in water measured at different time intervals and the corresponding optical photographs of $CsPbBr_3/CsPb_2Br_5$@ZIF-8@PMMA. (e) Schematic diagram of crystal structure and transformation process of $CsPbBr_3/CsPb_2Br_5$ HNCs.

tra also demonstrated that the encapsulation of ZIF-8 can effectively passivate the surface defects of $CsPbBr_3/CsPb_2Br_5$ HNCs through increasing binding energy of Pb-Br and lowering binding energy of Cs-Br in $CsPbBr_3/CsPb_2Br_5$@ZIF-8 (Fig. 3d) [39,18]. The XPS peak areas of Cs-Br decreases gradually from $CsPbBr_3$ NCs to $CsPbBr_3/CsPb_2Br_5$ HNCs and $CsPbBr_3/CsPb_2Br_5$@ZIF-8, and this phenomenon also implies the combination of Cs^+ with discrete $PbBr_6^{4-}$ to form $CsPbBr_3/CsPb_2Br_5$ HNCs. The Raman spectra of $CsPbBr_3$ and $CsPbBr_3/CsPb_2Br_5$ HNCs were compared in Fig. S3 (Supporting information). Two remarkable characteristic Raman vibrations of 84.8 and 144.3 cm^{-1} were observed for $CsPbBr_3$, in which the phonon vibration mode of TO_2 at 84.8 cm^{-1} is related to the vibration of $[PbBr_6]^{4-}$, whereas the broad low-intensity peak of 144.3 cm^{-1} corresponds to the phonon vibration mode of TO_3, mainly associated with the motion of Cs^+ ions [40]. Compared with $CsPbBr_3$, the left-shift of Raman peaks of $CsPbBr_3/CsPb_2Br_5$ and the enhancement of the peak at 140.1 cm^{-1} indicate the transformation of $CsPbBr_3$ into $CsPb_2Br_5$, further passivating the surface defects of $CsPbBr_3$ [41]. These Raman signals are not significant for $CsPbBr_3/CsPb_2Br_5$@ZIF-8 composite due to the encapsulation of ZIF-8.

The optical properties of $CsPbBr_3$ NCs, $CsPbBr_3/CsPb_2Br_5$ HNCs and $CsPbBr_3/CsPb_2Br_5$@ZIF-8 composite were investigated (Fig. 4a). The similar photoluminescence (PL) emission peak indicated that all of them had the same emission center, and compared with $CsPbBr_3$ NCs, $CsPbBr_3/CsPb_2Br_5$ HNCs has a narrower full width at half maximum and higher luminescence intensity than $CsPbBr_3$ NCs due to the passivation effect of $CsPb_2Br_5$ on halide vacancy defects. Additionally, due to the restriction of ZIF-8, the rates for photoinduced electron-hole recombination in $CsPbBr_3/CsPb_2Br_5$@ZIF-8 composite are restricted, supported by the corresponding weakened fluorescence intensity in comparison to $CsPbBr_3/CsPb_2Br_5$ HNCs [42]. Time-resolved photoluminescence (TRPL) was measured to investigate the dynamics of carrier transfer in $CsPbBr_3/CsPb_2Br_5$@ZIF-8 (Fig. 4b) with the detailed fitting data are listed in Table S2 (Supporting information). Average PL decay lifetimes of $CsPbBr_3$ NCs, $CsPbBr_3/CsPb_2Br_5$ HNCs, and $CsPbBr_3/CsPb_2Br_5$@ZIF-8 were 8.7, 36.6, and 14.1 ns, respectively. The $CsPbBr_3/CsPb_2Br_5$ HNCs shows an increased average PL lifetime, which implies that the formation of heterostructure passivated the non-radiative decay process of $CsPbBr_3$ NCs by increasing the recombination rate of carriers [24]. However, the fluorescence lifetime was reduced after encapsulation into ZIF-8, indicating that the migration rate of charge carriers was promoted in $CsPbBr_3/CsPb_2Br_5$@ZIF-8 composite.

Figs. 4c and d compared the water stability of the samples prior to the investigation of photocatalytic performance. The results showed that the luminescence of $CsPbBr_3$ NCs was completely quenched after soaking in water for 6 h due to the protective effect of surface hydrophobic ligands. After 16 h of immersion, the emission of $CsPbBr_3/CsPb_2Br_5$ HNCs was quenched because of the dissociation of $CsPb_2Br_5$ into $CsPbBr_3$ and $PbBr_2$ when immersed in water according to the following Eq. 1 [41]:

$$CsPb_2Br_5 \rightarrow Pb^{2+} + 2Br^- + CsPbBr_3 \quad (1)$$

In contrast, the fluorescence intensity of $CsPbBr_3/CsPb_2Br_5$@ZIF-8 composite remained nearly 40% after 42 h of immersion, which was attributed to the encapsulation and protective effect of the external ZIF-8. The corresponding PL spectra of these samples after immersing in water are shown in Fig. S4 (Supporting information). Although the water stability of $CsPbBr_3/CsPb_2Br_5$ HNCs packaged in ZIF-8 had been significantly improved, it was not enough to

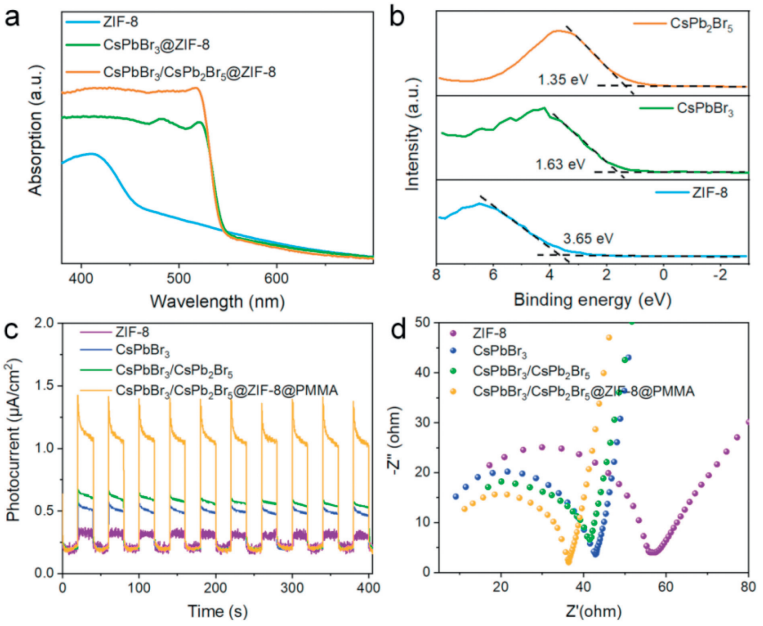

Fig. 5. (a) UV–vis absorption spectra, (b) VB-XPS spectra of ZIF-8, $CsPbBr_3$ and $CsPb_2Br_5$. (c) Measurement of transient photocurrent in response to on-off illumination. (d) EIS Nyquist plots of catalytic agent.

cope with harsh environmental erosion in practical applications. The PMMA polymer shelled $CsPbBr_3/CsPb_2Br_5$@ZIF-8 not only retained the excellent hydrophobicity of the polymer and the porosity of ZIF-8 (Fig. S5 in Supporting information), but also had superior water stability with improved enrichment performance towards organic pollutants. The $CsPbBr_3$@ZIF-8 composite was also prepared as a reference using the same procedure (Figs. S6 and S7 in Supporting information). Lacking the protection of $CsPb_2Br_5$ heterostructure, the fluorescence intensity of $CsPbBr_3$@ZIF-8 composite decayed dramatically after modification of PMMA. In stark contrast, the PL intensity of $CsPbBr_3/CsPb_2Br_5$@ZIF-8@PMMA composite was significantly enhanced compared to the initial intensity after 30 days of soaking in water due to the further passivation of $CsPb_2Br_5$ [34]. In detail, the $PbBr_6$ octahedron were formed in the process of $CsPbBr_3$ NCs growth, which can be transformed into $PbBr_8$ polyhedron in Pb-rich environment (Fig. 4e) [43,44]. Then, the $PbBr_8$ polyhedra shared top-angle Br atoms to produce a $[Pb_2Br_5]^-$ layer, and further bonded with Cs^+ to form $CsPb_2Br_5$. When the $CsPbBr_3/CsPb_2Br_5$@ZIF-8@PMMA composite was immersed in water, CsBr was stripped by water, and part of the $CsPbBr_3$ were decomposed to form $CsPb_2Br_5$ to further passivate the surface defects of $CsPbBr_3$, leading to a slight fluorescence enhancement. The characteristic XRD peaks of $CsPbBr_3$ and $CsPb_2Br_5$ remained for the composite (Fig. S8 in Supporting information), confirming its high water stability. Additionally, the intensity of the XPS signals of surface Pb^{2+} ions is weakened, while that of the crystal Pb^{2+} ions is enhanced after water treatment, indicating the reduce of surface defects in $CsPbBr_3$ accompanied by the formation of $CsPbBr_3/CsPb_2Br_5$ HNCs (Fig. S9 in Supporting information).

The UV–vis absorption spectra in Fig. 5a showed that pure ZIF-8 can only absorb light before 440 nm with a band gap of 4.06 eV (Fig. S10 in Supporting information), wasting a lot of visible light resources. In contrast, all of $CsPbBr_3$@ZIF-8, $CsPbBr_3/CsPb_2Br_5$@ZIF-8 and $CsPbBr_3/CsPb_2Br_5$@ZIF-8@PMMA composites can extend the light utilization range to 520 nm. The $CsPbBr_3/CsPb_2Br_5$ HNCs and $CsPbBr_3/CsPb_2Br_5$@ZIF-8@PMMA exhibit the best light absorption intensity, showing great potential for photocatalytic application. The valence band (VB) position of ZIF-8, $CsPbBr_3$ and $CsPb_2Br_5$ was estimated using the VB-XPS spectra (Fig. 5b), which can be calculated by Eq. 2:

$$E_{VB(NHE)} = \varphi + E_{VB-XPS} - 4.44 \quad (2)$$

where $E_{VB(NHE)}$ is the VB potential of a standard hydrogen electrode, $E_{VB\text{-}XPS}$ is the VB value measured by VB-XPS, and φ is the work function of the XPS analyzer (4.2 eV) [45–47]. Therefore, the $E_{VB(NHE)}$ of ZIF-8, $CsPbBr_3$ and $CsPb_2Br_5$ is determined to be 3.41, 1.39 and 1.11 eV (*vs.* NHE), respectively. XRD patterns demonstrate the pure phase of the prepared $CsPbBr_3$ and $CsPb_2Br_5$ (Fig. S11 in Supporting information). Moreover, the photoelectrochemical test was used to investigate the charge transport efficiency of photogenerated carriers. As demonstrated in Fig. 5c, all samples displayed a consistently stable photoresponse for 10 light-on/off cycles. The photocurrent response of $CsPbBr_3/CsPb_2Br_5$@ZIF-8@PMMA was remarkably higher than the other samples. The increased photocurrent suggests a significant reduction of the charge transfer resistance of the sample, demonstrating that the formation of $CsPbBr_3/CsPb_2Br_5$ HNCs and the encapsulation of ZIF-8 promoted internal carrier transport [13]. Similarly, the typical Nyquist plots from Electrochemical impedance spectroscopy (EIS) showed that the $CsPbBr_3/CsPb_2Br_5$@ZIF-8@PMMA composite has the smallest arc radius, indicating the lowest charge transfer resistance and high charge transfer rate (Fig. 5d).

The photocatalytic property of $CsPbBr_3/CsPb_2Br_5$@ZIF-8@PMMA was then investigated by degradation of TCH under visible light irradiation ($\lambda > 400$ nm). Typically, 50 mL 40 mg/L TCH aqueous solution and 20–50 mg $CsPbBr_3/CsPb_2Br_5$@ZIF-8@PMMA were mixed in a quartz reactor. After that, the mixed solution was stirred without light for 30 min to achieve an adsorption/desorption balance between the TCH and the catalysts. An equal amount of solution was centrifuged at different time intervals to remove the photocatalyst. The pH of the photocatalytic reaction solution is close to neutral. The characteristic peaks were detected using UV–vis spectrophotometer and the concentration changes in the range of 230–500 nm were determined (Fig. S12 in Supporting information). Fig. 6a displays the concentration (C/C_0) variation plots of different photocatalysts. Before photocatalysis, the catalyst powder was magnetically stirred for 30 min to achieve the adsorption-

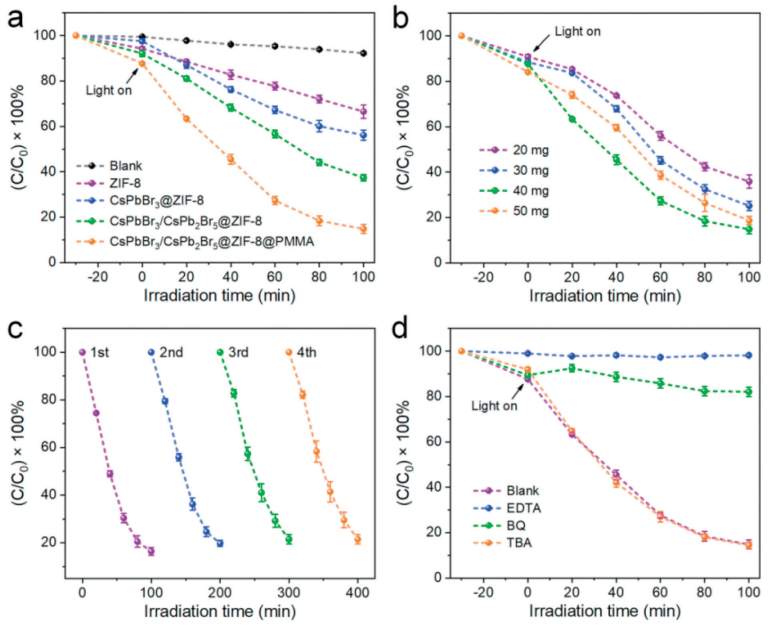

Fig. 6. (a) Time-dependent absorption spectra of TCH aqueous solution under visible light irradiation ($\lambda > 400$ nm, $m_{catalyst} = 40$ mg). (b) Plot of C/C_0 as a function of irradiation time using varying amounts of $CsPbBr_3/CsPb_2Br_5$@ZIF-8@PMMA catalysts: 20, 30, 40, and 50 mg. (c) Four cycles of photo-degradation of TCH over $CsPbBr_3/CsPb_2Br_5$@ZIF-8@PMMA. (d) The effect of several trapping reagents on photocatalytic degradation.

desorption equilibrium of pollutant. Only 7.8% of TCH was self-degraded after 100 min with the absence of any photocatalyst. When ZIF-8 was added as a photocatalyst, the degradation rate reached only 33.1% in 100 min. $CsPbBr_3$@ZIF-8 was also tested as a reference under the same condition with a degradation rate of 44.8%. The $CsPbBr_3/CsPb_2Br_5$@ZIF-8 photocatalyst has a degradation efficiency of about 63.7%. Different $CsPbBr_3/CsPb_2Br_5$@ZIF-8@PMMA composites were prepared by adjusting the mass ratio of $CsPbBr_3/CsPb_2Br_5$@ZIF-8 to PMMA (Fig. S13 in Supporting information). The results proved that the highest degradation rate can up to 87.2% when the mass ratio of $CsPbBr_3/CsPb_2Br_5$@ZIF-8 to PMMA was 1:3.

The effect of the dosage of $CsPbBr_3/CsPb_2Br_5$@ZIF-8@PMMA composite on the photocatalytic degradation of TCH were further studied. With the increase of photocatalyst from 20 mg to 40 mg, the TCH degradation efficiency is also increased (Fig. 6b). Nevertheless, when the photocatalyst mass reaches up to 50 mg, the photocatalytic efficiency decreased slightly, which may be caused by the aggregation of catalyst. The cyclic stability of photocatalysts is crucial in evaluating their performance, and which was assessed by measuring the degradation of TCH over four consecutive runs. Fig. 6c demonstrates that the $CsPbBr_3/CsPb_2Br_5$@ZIF-8@PMMA can maintain photocatalytic activity even after 4 cycles, indicating its good durability. Moreover, we measured the XRD pattern after 5 cycles of degradation, which revealed no significant miscellaneous peaks (Fig. S14 in Supporting information). Photogenerated $^{\bullet}O_2^-$, holes (h^+) and $^{\bullet}OH$ are crucial in photodegradation. Trapping experiments were conducted to determine which radical dominates during the photocatalytic degradation of TCH to enhance the comprehension of photocatalytic mechanism (Fig. 6d). Benzoquinone (BQ), ethylenediaminetetraacetic acid disodium salt (EDTA-2Na), and *tert*–butanol (TBA) are selected as radical trappers for $^{\bullet}O_2^-$, h^+, and $^{\bullet}OH$, respectively (Fig. S15 in Supporting information). The TCH degradation efficiency decreased when the quencher of EDTA and BQ were introduced, demonstrating that h^+ and $^{\bullet}O_2^-$ species play dominant roles in TCH degradation.

The energy band structures of the cubic phase $CsPbBr_3$ and tetragonal phase $CsPb_2Br_5$ were calculated using DFT, and the results demonstrates that the $CsPbBr_3$ is a direct bandgap semiconductor with a small bandgap of 1.754 eV and the $CsPb_2Br_5$ is an indirect bandgap semiconductor with a large bandgap of 3.049 eV (Figs. 7a and b). The above theoretically calculated bandgap value of $CsPb_2Br_5$ is consistent with the experimental finding (E_g, 3.13 eV), whereas the fitted bandgap of $CsPbBr_3$ is slightly lower than that of the experimental E_g value (2.28 eV) (Fig. S16 in Supporting information) [24]. Accordingly, the E_{CB} was determined to be −0.65, −0.89 and −2.02 eV (*vs.* NHE) for ZIF-8, $CsPbBr_3$ and $CsPb_2Br_5$, respectively, using the equation of $E_{VB} = E_g + E_{CB}$. Based on the comprehensive findings from the reported literature, the findings revealed that the typical type-II heterojunction was constructed between $CsPbBr_3$ and $CsPb_2Br_5$, and the Z-scheme heterojunction was formed between $CsPb_2Br_5$ and ZIF-8 (Fig. 7c) [13,42]. When high-energy light irradiated $CsPbBr_3/CsPb_2Br_5$@ZIF-8@PMMA, electrons in the valence bands of $CsPbBr_3$, $CsPb_2Br_5$, and ZIF-8 were excited and jumped to the conduction bands, producing photoelectrons (e^-) and leaving corresponding photoholes (h^+) in the valence bands. Due to the construction of the type-II heterojunction, photoelectrons on the conduction band of $CsPb_2Br_5$ would be transferred to $CsPbBr_3$. Similarly, the photoelectrons in the conduction band of ZIF-8 transferred to recombine with the holes in the valence band of $CsPb_2Br_5$ on accounts of the formation of Z-scheme heterojunction, which lead to separation of photogenerated electrons and holes. At the moment, the $CsPbBr_3$ conduction band gathered electrons and then activated O_2 to form superoxide radicals ($^{\bullet}O_2^-$); the holes that accumulated on the valence band of ZIF-8 reacted with H_2O to form hydroxyl radicals ($^{\bullet}OH$). The maximum separation efficiency of photoelectrons and holes was achieved in this reaction system, promoting the photocatalytic TCH degradation.

In summary, we judiciously prepared an ultrastable $CsPbBr_3/CsPb_2Br_5$@ZIF-8@PMMA composite by capitalizing on the confinement effect of ZIF-8 and controlling the ratio of Cs^+/Pb^{2+} precursors through thermal injection process, and then modifying the surface of ZIF-8 with hydrophobic polymer PMMA. Detailed characterizations confirmed the effective construction of the type-II heterojunction between $CsPbBr_3$ and $CsPb_2Br_5$

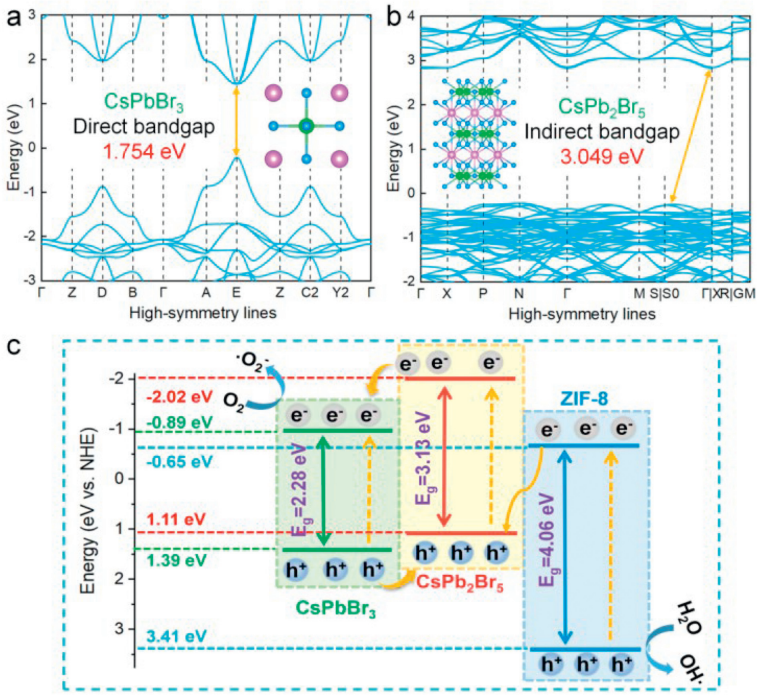

Fig. 7. The energy band structures of (a) $CsPbBr_3$ and (b) $CsPb_2Br_5$. (c) Mechanism diagram of the $CsPbBr_3/CsPb_2Br_5$@ZIF-8@PMMA photocatalyst for TCH photo-degradation.

and its accelerated charge transfer and separation. Moreover, the Z-Scheme heterostructure constructed by the introduction of ZIF-8 not only further accelerated the charge separation, but also improved the enrichment of TCH pollutants. Thanks to the unique band structure combining type-II and Z-scheme, the obtained catalyst showed excellent visible-light-driven photodegradation performance towards TCH in aqueous solution with a high degradation efficiency of ~87%. The catalyst also exhibits exceptional stability and reusability. Furthermore, the mechanism of the photocatalytic reaction was analyzed in detail. This research provides new insights for fabricating and realizing the application of new $CsPbBr_3$-based photocatalyst in aqueous phase photocatalysis.

Declaration of completing interest

The authors declare that they have no known competing financial interests or personal relationships that could have appeared to influence the work reported in this paper.

CRediT authorship contribution statement

Le Han: Writing – original draft, Methodology, Formal analysis, Data curation. **Zhou Yuan:** Formal analysis. **Bohan Li:** Data curation. **Yuchi Zhang:** Formal analysis. **Lin Yang:** Data curation. **Yan Xu:** Writing – review & editing, Supervision, Project administration, Funding acquisition, Conceptualization.

Acknowledgments

The present work was supported by National Natural Science Foundation of China (No. 22171040), Shenyang Young and Middle-aged Science and Technology Innovation Talent Support Program (No. RC230784), Guangdong Basic and Applied Basic Research Foundation (No. 2023A1515140011), and Fundamental Research Funds for the Central Universities, China (No. N2305017).

Supplementary materials

Supplementary material associated with this article can be found, in the online version, at doi:10.1016/j.cclet.2024.110349.

References

[1] L. Duan, L. Hu, X. Guan, et al., Adv. Energy Mater. 11 (2021) 2100354.
[2] L. Protesescu, S. Yakunin, M.I. Bodnarchuk, et al., Nano Lett. 15 (2015) 3692–3696.
[3] K. Li, S. Li, W. Zhang, et al., J. Colloid Interface Sci. 596 (2021) 376–383.
[4] H. Zhou, Y. Qu, T. Zeid, et al., Energy Environ. Sci. 5 (2012) 6732–6743.
[5] D. Cardenas-Morcoso, A.F. Gualdrón-Reyes, A.B.F. Vitoreti, et al., J. Phys. Chem. Lett. 10 (2019) 630–636.
[6] G. Gao, Q. Xi, H. Zhou, et al., Nanoscale 9 (2017) 12032–12038.
[7] K. Xie, S. Wei, A. Alhadhrami, Adv. Compos. Hybrid Mater. 5 (2022) 1423–1432.
[8] J. Zheng, Y. Zhang, C. Jing, et al., Adv. Compos. Hybrid Mater. 5 (2022) 2406–2420.
[9] T. Ghosh, S. Aharon, A. Shpatz, et al., ACS Nano 12 (2018) 5719–5725.
[10] J. Chen, D. Liu, M.J. Al-Marri, et al., Sci. China Mater. 59 (2016) 719–727.
[11] T. Ji, H. Zhang, S.J. Shah, et al., J. Mater. Chem. A 10 (2022) 22571–22583.
[12] T. Liang, W. Liu, X. Liu, et al., Chem. Mater. 33 (2021) 4948–4959.
[13] L. Ding, B. Borjigin, Y. Li, et al., ACS Appl. Mater. Interfaces 13 (2021) 51161–51173.
[14] S. Bera, N. Pradhan, ACS Energy Lett. 5 (2020) 2858–2872.
[15] A.M. Smith, S. Nie, Acc. Chem. Res. 43 (2010) 190–200.
[16] G.H. Ahmed, J. Yin, O.M. Bakr, et al., ACS Energy Lett. 6 (2021) 1340–1357.
[17] D.N. Dirin, B.M. Benin, S. Yakunin, et al., ACS Nano 13 (2019) 11642–11652.
[18] G. Jiang, C. Guhrenz, A. Kirch, et al., ACS Nano 13 (2019) 10386–10396.
[19] V.K. Ravi, S. Saikia, S. Yadav, et al., ACS Energy Lett. 5 (2020) 1794–1796.
[20] J. Shamsi, Z. Dang, P. Ijaz, et al., Chem. Mater. 30 (2018) 79–83.
[21] G. Kaur, K. Justice Babu, et al., J. Phys. Chem. Lett. 10 (2019) 5302–5311.
[22] B. Wang, C. Zhang, S. Huang, et al., ACS Appl. Mater. Interfaces 10 (2018) 23303–23310.
[23] I. Rosa-Pardo, A. Ciccone, R. Arenal, et al., Chem. Mater. 35 (2023) 7011–7019.
[24] C. Zhang, Z. Wang, M. Wang, et al., ACS Appl. Mater. Interfaces 15 (2023) 35216–35226.
[25] P. Gao, Z. Cui, X. Liu, et al., Chem. Eur. J. 28 (2022) e202201095.
[26] P. Chen, W.J. Ong, Z. Shi, et al., Adv. Funct. Mater. 30 (2020) 1909667.
[27] H. Huang, D. Verhaeghe, B. Weng, et al., Angew. Chem. 134 (2022) e202203261.
[28] E.M. Akinoglu, D.A. Hoogeveen, C. Cao, et al., ACS Nano 15 (2021) 7860–7878.
[29] J. Li, H. Wang, X. Yuan, et al., Coord. Chem. Rev. 404 (2020) 213116.
[30] H. Dai, X. Yuan, L. Jiang, et al., Coord. Chem. Rev. 441 (2021) 213985.
[31] W. Mo, Z. Fan, S. Zhong, et al., Small 19 (2023) 2207705.
[32] M. He, Q. Zhang, F. Carulli, et al., ACS Energy Lett. 8 (2023) 151–158.
[33] L. Han, Y. Han, J. Wu, et al., Mater. Chem. Front. 5 (2021) 7843–7851.
[34] L. Han, B. Li, Y. Zhang, et al., Chem. Eng. J. 473 (2023) 145323.

[35] X.C. Yang, S.Q. Fu, Q.L. Li, et al., Chem. Eng. J. 465 (2023) 142869.
[36] A. Mohammadi, A.N. Pour, J. CO_2 Util. 69 (2023) 102424.
[37] Z.G. Ayanoğlua, M. Doğan, Diam. Relat. Mater. 108 (2020) 107950.
[38] D. Yang, X. Li, Y. Wu, et al., Adv. Opt. Mater. 7 (2019) 1900276.
[39] W. Wang, R. Guo, X. Xiong, et al., Mater. Today Phys. 18 (2021) 100374.
[40] D. Han, K. Yang, C. Bai, et al., Chem. Eng. J. 475 (2023) 146209.
[41] Y. Ding, S. Maitra, C. Wang, et al., Interdiscip. Mater. 1 (2022) 213–255.
[42] Y. Hou, F. Meng, J. He, et al., J. Mater. Chem. C 11 (2023) 13570–13578.
[43] B. Qiao, P. Song, J. Cao, et al., Nanotechnology 28 (2017) 445602.
[44] G. Li, H. Wang, Z. Zhu, et al., Chem. Commun. 52 (2016) 11296–11299.
[45] X. Li, Q. Liu, F. Deng, et al., Appl. Cataly. B: Environ. 314 (2022) 121502.
[46] F. Yu, T. Huo, Q. Deng, et al., Chem. Sci. 13 (2022) 754–762.
[47] H. Li, F. Yu, A. Li, et al., Chem. Eng. J. 489 (2024) 151219.